Journal of the Brazilian Society of Mechanical Sciences and Engineering (2024) 46:591
https://doi.org/10.1007/s40430-024-05177-2

TECHNICAL PAPER

Optimized design of car frontal bumper with aluminum foam sandwich structure under low velocity impacts

Ali Afrasiabi[1] · **Hossein Mohammadi**[1] · **Kamyar Hashemnia**[1]

Received: 18 April 2024 / Accepted: 29 August 2024

Abstract

This study introduces a novel sandwich structure absorber for car bumpers, utilizing thin layers of aluminium foam. This absorber improves energy absorption and impact resistance. This research compares the novel absorber to a conventional polymer-integrated model, by examining impact force, von-Mises stress, equivalent plastic strain, energy absorption, and coefficient of restitution. Utilizing the finite element method, the effects of shell density and thickness are analysed under E.C.E-R042 low-velocity impact standards. Sandwich absorbers exhibit lower stresses and plastic strains in the core. In addition, they demonstrate smaller impact forces and enhanced energy absorption within a specific range of shell densities. Furthermore, the absorber's flexibility strongly influences contact time. The core of sandwich absorber models accounts for between 70 and 90% of energy absorption, indicating slightly lower energy absorption than polymer foams. The simulation results are analysed using analysis of variance to investigate the combined effect of the density and thickness of the sandwich absorber shell on the efficiency of the sandwich absorber. The optimal values of density and thickness are determined using grey relation analysis to be 150 kg/m^3 and 25 mm, respectively.

Keywords Sandwich structure · Finite element modeling · Low velocity impact · Car bumper absorber · Aluminum foam · Taguchi method · Analysis of variance

1 Introduction

The automotive industry conducts extensive research to enhance the quality, design, and use of premium materials. The car bumper system is a vital component that plays a significant role in reducing the risk of damage to the car and passengers during collisions. Material selection and design are critical factors, with cost and weight being the most significant considerations for creating a crash-worthy and cost-effective bumper [1, 2]. In recent years, the increase in road accidents could be attributed to various factors, including non-standard road construction and driver inattentiveness during parking, as the number of vehicles on the road continues to rise [3]. Low-speed collisions are a significant concern during heavy traffic or parking due to slow movement. However, some bumpers may not be designed appropriately to prevent damage to various parts of the vehicle during these collisions or absorb the collision's energy effectively enough to prevent vehicle damage [4]. The absorber in the bumper system plays a crucial role in absorbing energy during collisions and are typically made of compressed polymer foams [5, 6].

Metal foams are composed of interconnected networks and categorize into closed and open cells. Closed cells offer significant potential in various industries, including automobiles and aerospace. Aluminum, steel, nickel, copper, zinc, titanium, and magnesium could be used as base materials for metal foams. Aluminum is the most commonly used metal due to its lightweight, toughness, corrosion resistance, and low melting point. Metal foams have unique properties, including high resistance, low density, and acoustic and thermal insulation. Pure metals and their alloys are not the only options for selecting base materials for the foams [7, 8]. Deshpande and Fleck [9] undertook a pioneering investigation into the strength of aluminum alloy foams, specifically Alporas and Duocel. Their exploration of the yield surface revealed the material's strength under various

Technical Editor: João Marciano Laredo dos Reis.

✉ Kamyar Hashemnia
khashemnia@shirazu.ac.ir

[1] School of Mechanical Engineering, Shiraz University, Molla Sadra St., Shiraz, Iran

Published online: 06 September 2024

compressive stresses. Going beyond aligning experiments with predictions, their research introduced a simplified model, providing valuable insights into foam behavior and laying a solid foundation for understanding stress responses in alloy foams. Deshpande and Fleck [10] studied the cores of sandwich beams and found that both pyramidal and tetrahedral cores showed the same normal stiffness and the same shear properties under the same conditions. It could be said that the degree of anisotropy in shear strength was higher in the pyramidal core. Davoodi et al. [11, 12] found that using epoxy composite cushions with reinforced fibers were more effective than foam absorbers for reducing pedestrian injuries in car accidents. Another study compared 8 bumper beam cross-sections and determined the most appropriate one using low-speed impact tests in Abaqus software. Beyene et al. [13] developed a high-performance bumper that utilized glass mat thermoplastic (GMT) composites and an innovative pattern to outperform steel bumpers in strength and functionality. To evaluate the bumper's effectiveness, they conducted simulations of its performance in Abaqus software and compared its energy absorption, impact force, and damage incurred. Xiao et al. [14] evaluated foam-filled bumpers and found that functionally graded foam (FGF) and urea–formaldehyde (UF) foam improved energy absorption, with FGF foam performing better than UF foam. Diaz-Alvarez et al. [15] studied bumper beams made of biocomposites and found that fiber type played a key role in controlling the maximum collision force. Archakam and Muthuswamy [16] focused on enhancing vehicle safety by designing an integrated collision energy absorption system with a magneto-rheological absorber (MRA). They tested 6 models to evaluate their safety and found that 3 with MRA outperformed the one without MRA. Wang et al. [17] conducted a comprehensive analysis of closed-cell aluminum foams using both uniaxial and biaxial tests at elevated temperatures. Their findings revealed linear associations between drop stress/initial failure strength and temperature. The research introduced a rate-dependent constitutive model, establishing connections among compressive strength, strain rate, and densification strain. The proposed crushable foam model, incorporating yield ratio input, aligned well with experimental results, offering valuable insights into the mechanical behavior of metal foams in challenging conditions. Examining the crashworthiness of Aluminum foam-filled open-hole tubes (AFOTS), Hou et al. [18] optimized the bumper beam design using fiber metal laminates (FML) and a corrugated sandwich structure, resulting in improved performance under low-speed impact. Lopez et al. [19] identified structural vulnerabilities in passenger vehicles during frontal collisions through experimental and numerical results. Their noteworthy achievement underscored the urgency for innovative design interventions to rectify these issues, aiming to align with the E.C.E-R029 safety standard and enhance driver safety in frontal accidents. Liu et al. [20] successfully enhanced the mechanical properties of Aluminum foam (AF) by introducing a combined approach of melt foaming and infiltration casting, leading to improved energy absorption, specific energy absorption, and specific resistance in bicontinuous interpenetrating porous composites (BIPCs). Skeens and Kyriakides [21] conducted experiments on a polymer closed-cell foam (relative density 0.077) subjected to axial and external pressure. Their findings revealed a clear stress-displacement response, demonstrating linear decreases in initial stresses and plateau with rising external pressure.

Previous research investigated the behavior of aluminum foam and its effects on various structures using experiments and finite element simulations. Markaki and Klein [22] examined the cell wall structure of metal foams and its impact on foam mechanical properties. They tested foams with different cell structures and similar densities under various loadings to evaluate the foam's change of state, yielding, and crushing mechanisms. Zarei and Kruger [23] conducted impact bending tests and numerical simulations on an aluminum beam with and without foam. The study found that the foam-filled beam had higher bending strength than the hollow one. Shen et al. [24] investigated the strain rate sensitivity of Alporas foam and its behavior under compressive loading at different rates. Their study provided valuable insights into the mechanics of foams and their energy absorption capabilities, with implications for the design and optimization of impact-resistant materials. Yang et al. [25] explored the energy absorption capability of polymer foams in bumper systems and found that repeated compressive loadings significantly reduced their performance. Hassanli and Paydar [26] analyzed the effect of structural design on the mechanical properties and energy absorption capability of powder metallurgy-produced aluminum foams with a relative density range of 0.28–0.48. Gomes et al. [27] used the nonlinear finite element method to analyze the impact behavior of a sandwich structure with an agglomerated cork core, providing insights into the design of impact-resistant materials. Liu et al. [28] analyzed 14 test samples of sandwich panels featuring a stainless steel front shell, a steel alloy back shell, and an aluminum foam core. The findings indicated a noteworthy impact of the front shell, back shell, and aluminum foam thickness on both bearing capacity and energy absorption of the sandwich panels. Jalali et al. [29] successfully employed machine learning models to precisely estimate 4 crucial damage properties (longitudinal modulus, tensile strength, compressive strength, in-plane shear strength) of glass/epoxy sheets subjected to low-velocity impacts, with the results aligning closely (within 4%–6%) with experimental data.

The current study's main objective is to enhance bumpers performance by introducing a new model that incorporates modifications in both the absorber material composition

and geometric design. The authors developed an innovative structure using thin shells of aluminum foam and compared it to the primary model of the absorber that had a polymer integrated structure. based on factors such as maximum impact force, maximum von Mises stress, maximum equivalent plastic strain, absorbed energy, and coefficient of restitution. To validate their approach, the authors conducted 3D-FEM simulation tests, providing insights into the development and optimization of impact-resistant materials for automotive applications.

After introduction, in Sect. 2, the article delves into introducing the theoretical basis of the research. This encompasses the relationships governing both the core problem and the behavior of foams. Moving on to Sect. 3, it outlines the simulation methodology applied to address the problem. This includes an overview of the materials, boundary conditions, contacts, and the specific cases simulated. Section 4 focuses on the validation of the problem. Section 5 provide an in-depth analysis of the extracted results and in the last Section, the obtained conclusions are generally stated.

2 Theory

2.1 Impact force and energy absorption

There is a certain amount of deformation during a collision depending upon the rate of change of the relative velocity normal component, which is due to the impact force. When 2 objects come into contact with each other, a contact area forms between them, which is very small in size compared to the rest of the body and therefore, it is shown by contact point C (Fig. 1). The resulting impact force between 2 objects B and $B\prime$ were formulated by Newton's second law as shown in Eq. (1) where δ is the relative displacement between 2 bodies (Eq. (2)) caused by the impact force F_{imp} [30].

$$F_{imp} = -m_B \frac{d^2\delta_B}{dt^2} = -m_{B\prime} \frac{d^2\delta_{B\prime}}{dt^2}, \tag{1}$$

$$\delta = \delta_B + \delta_{B\prime}. \tag{2}$$

As a result of applying a load to an object, strains are created inside the object, which increase the level of energy inside it. The amount of energy absorbed by an object is calculated from Eq. (3),

$$E = \int_0^s F ds, \tag{3}$$

where E, s and F are the absorbed energy, deformation and force, respectively. By dividing the amount of energy absorbed by an object by its mass M, the specific absorbed energy for an object is obtained by Eq. (4) [24, 27, 28].

$$E_s = \frac{E}{M}. \tag{4}$$

2.2 Foam modeling

Foams could be modelled in a variety of ways. In this research, the crushable foam model with isotropic hardening is used. Considering the plastic behavior of foams, in the crushable foam model with isotropic hardening, the yield function is represented by an ellipse in the stress plane for the crushable foam model with isotropic hardening (Fig. 2) [9, 22, 27, 31].

In Eq. (5), the yield surface with isotropic hardening is expressed,

$$F = \sqrt{q^2 + \alpha^2 p^2} - B^2 = 0, \tag{5}$$

$$p = -\frac{1}{3} trace\boldsymbol{\sigma}, \tag{6}$$

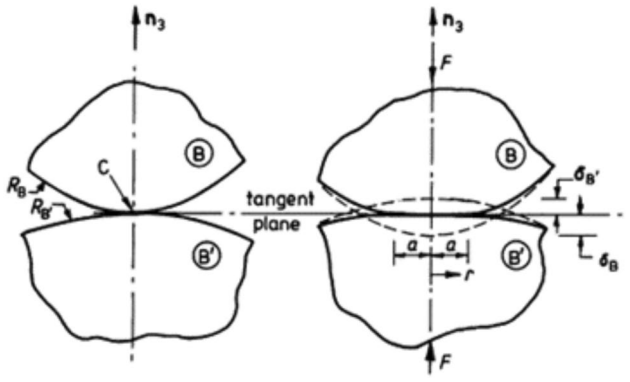

Fig. 1 The schematic view of objects B and $B\prime$ colliding with each other [30]

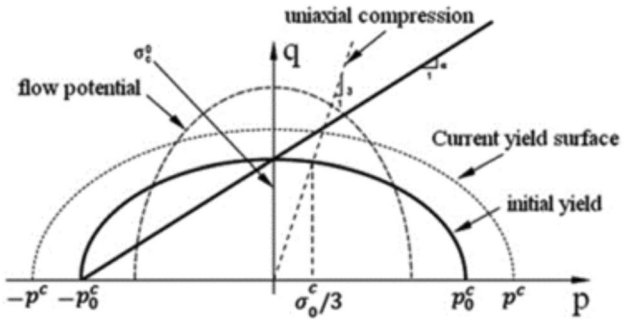

Fig. 2 Schematic of yield surface and flow potential in the p-q stress plane for crushable foam with isotropic hardening [32]

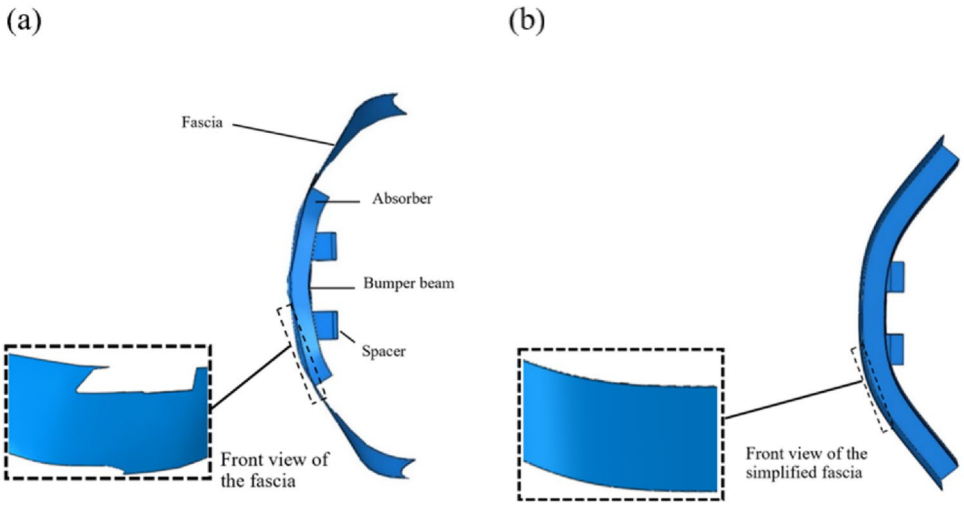

Fig. 3 Schematic of the designed bumper system before and after simplification, as shown in **a** and **b**, respectively. Part **a** shows the main components of the bumper system

$$q = \sqrt{\frac{3}{2}\boldsymbol{S} : \boldsymbol{S}}; \boldsymbol{S} = \boldsymbol{\sigma} + p\boldsymbol{I}, \tag{7}$$

$$B = \alpha P_c, \tag{8}$$

$$\alpha = \frac{3K}{\sqrt{9 - K}}, \tag{9}$$

$$K = \frac{\sigma_0^c}{P_0^c}, \tag{10}$$

where F, p and q are yield surface, mean compressive stress (Eq. (6) and von Mises stress, respectively. $\boldsymbol{\sigma}$ is the stress tensor and $\mathbf{S}$ is the deviatoric stress tensor, (Eq. (7)). Also, B specified the size of the q-axis of the yield surface (Eq. (8)). P_c is the yield strength under the hydrostatic pressure condition and σ_c shows the absolute value of yield strength under the uniaxial compression condition. The shape factor, α, affects the elongation of the ellipse yield surface or p-axis (Eq. (9)). In Eq. (10), K is called the stress ratio, which is obtained by dividing σ_0^c by P_0^c being the initial yield stresses under uniaxial compression and under hydrostatic pressure, respectively. Also K must be in the range $0 < K < 3$ [27, 31, 32].

Flow potential in the isotropic hardening model, G, is expressed in Eq. (11),

$$G = \sqrt{q^2 + \beta^2 p^2}, \tag{11}$$

$$\beta = \frac{3}{\sqrt{2}}\sqrt{\frac{1 - 2\upsilon_p}{1 + \upsilon_p}}, \tag{12}$$

Table 1 Thickness and material of different components of the front bumper system

Bumper system component	Material	Thickness (mm)
Fascia	HDPE	3.10
Absorber	EPP foam	100
Bumper beam	Al2024-T3	2.45
Spacer	Al2024-T3	1

Table 2 Material properties of HDPE and Al2024-T3

Material	Modulus of elasticity (GPa)	Poisson's ratio	Density (kg/m^3)	Yield strength (MPa)
HDPE [40]	1.18	0.46	950	25.40
Al2024-T3 [41]	70	0.30	2770	391

$$\upsilon_p = \frac{3 - K^2}{6}, \tag{13}$$

where parameter β shows the shape of the flow potential, which is oval in the stress plane (Eq. (12)). υ_p is called plastic Poisson's ratio expressed as the ratio of plastic strains in transverse and longitudinal directions under uniaxial compressive loading and its value is in the interval $(-1,0.5)$. For most foams with low density, υ_p is close to zero and $\beta \approx 2.12$. Equation (13) expresses the relation of plastic Poisson's ratio to the stress ratio [32].

It is possible to determine the modulus of elasticity of foams using 2 methods [33]:

In the first method, by assuming that $\upsilon_p \approx 0$, by obtaining the slope of the line of the elastic part of the foam stress–strain diagram, its modulus of elasticity, E_f, could

be obtained. In the second method Eq. (14) is specific to the modulus of elasticity of the metal foams.

$$E_f = AE_a\overline{\rho}^2, \tag{14}$$

$$\overline{\rho} = \frac{\rho_f}{\rho_a} = 1 - p_r, \tag{15}$$

The parameter A in Eq. (14) is obtained from the uniaxial pressure test on metal foams, which indicates the plastic behavior of the metal foam. E_a and $\overline{\rho}$ are the modulus of elasticity of the base metal and the relative density of the foam, respectively. The relative density was calculated by dividing the density of the foam (ρ_f) by the density of the base metal (ρ_a) and it also related to the foam porosity, p_r, as in Eq. (15) [33].

2.3 Grey relational analysis (GRA)

This study employs the gray relational analysis (GRA) method to investigate the effects of several parameters on the output response. GRA determines the optimal value for each parameter by converting them into variables, followed by simulation or testing, and then extracting the relevant parameters. This approach not only identifies the optimal value for each parameter but also examines the interactions between them, providing a comprehensive understanding of their combined impact on the output response. By using

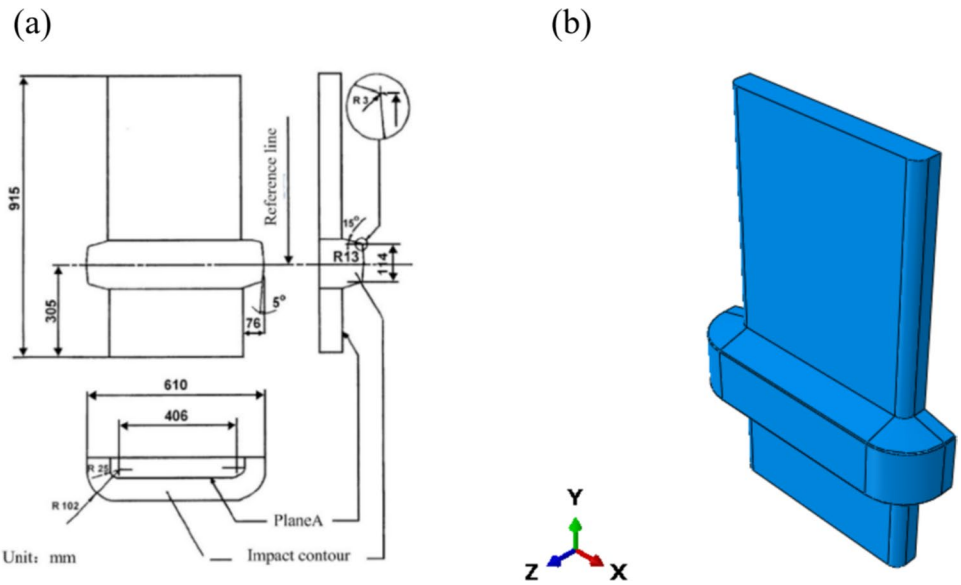

Fig. 4 **a** Three views of the impactor [38] and, **b** a 3D scheme of the impactor

Table 3 Material properties of an absorber bumper system with a sandwich structure

Material	Modulus of elasticity (MPa)	Poisson's ratio	Plastic Poisson's ratio	Density (kg/m^3)	Stress ratio	Yield strength (MPa)
EPP foam [42]	5.132	0	0	70	1.732	0.25
Low density Aluminumfoam [43]	300	0.3	0.05	150	1.558	0.93
High density Aluminumfoam [43]	1500	0.3	0.05	300	1.558	4.41

Table 4 Listing the abbreviated names and descriptions of the models examined in this study

Abbreviated name	Complementary definition
Simple	Absorber with a simple structure without a shell
SanX-Y	Absorber with a sandwich structure, the thickness and density of the shell are X mm and Y kg/m^3, respectively
HybridX	Absorber with a sandwich structure—shell thickness X mm—in this research, half of the shell thickness has a density of 150 and the other half has a density of 300 kg/m^3

GRA, we can optimize decision-making in complex systems where multiple factors influence the outcomes [34].

This method was first introduced and developed in research [35]. The first step in using the GRA method involves normalizing the data between 0 and 1 to create a gray relationship. Then Eqs. (16) and (17) are used to determine the optimal value for each parameter based on whether a larger or smaller value is more desirable, respectively. This approach makes it possible to determine an optimal value for each parameter while also considering the interactions between them [34].

$$x_{ij} = \frac{y_{ij} - min_j y_{ij}}{max_j y_{ij} - min_j y_{ij}}; i = 1, 2, \ldots, aj = 1, 2, \ldots, b \tag{16}$$

$$x_{ij} = \frac{max_j y_{ij} - y_{ij}}{max_j y_{ij} - min_j y_{ij}}; i = 1, 2, \ldots, aj = 1, 2, \ldots, b \tag{17}$$

where a and b represent the number of simulations or experiments performed and the number of effective parameters in each simulation or experiment, respectively. x_{ij} is the value after generating the gray relation, and y_{ij} is the original alternative in the i th simulation for the j th parameter. x_{0j} is the most ideal normalized option among all simulations for the j th parameter. In the next step, to show how close x_{ij} is to x_{0j}, the gray relational coefficient (GRC) is used, which is expressed in Eq. (18). A larger GRC indicates a value closer to x_{0j} [36].

$$\xi_{ij} = \frac{\Delta_{min} + \zeta \Delta_{max}}{\Delta_{0ij} + \zeta \Delta_{max}}; \zeta \in [0, 1] \tag{18}$$

$$\Delta_{0ij} = \left| x_{0j} - x_{ij} \right| \tag{19}$$

The distinguishing coefficient ζ is usually assigned a value of 0.5 in calculations [34]. Δ_{min} and Δ_{max} represent, respectively, the minimum and maximum values of Δ_0 among all simulations for the j th parameter. A higher GRC means the parameter's greater proximity to the optimal value. GRG is calculated using Eq. (20) after determining the GRC.

$$\gamma_i = \sum_{j=1}^{b} \omega_j \xi_{ij} \tag{20}$$

In Eq. (20), $\sum_{j=1}^{b} \omega_j = 1$, where ω_j is the weighting factor for the j th parameter. By converting multiple GRCs into a single gray relational grade (GRG) for each simulation, it can be determined that a higher GRG corresponds to closer proximity to the optimal state [37].

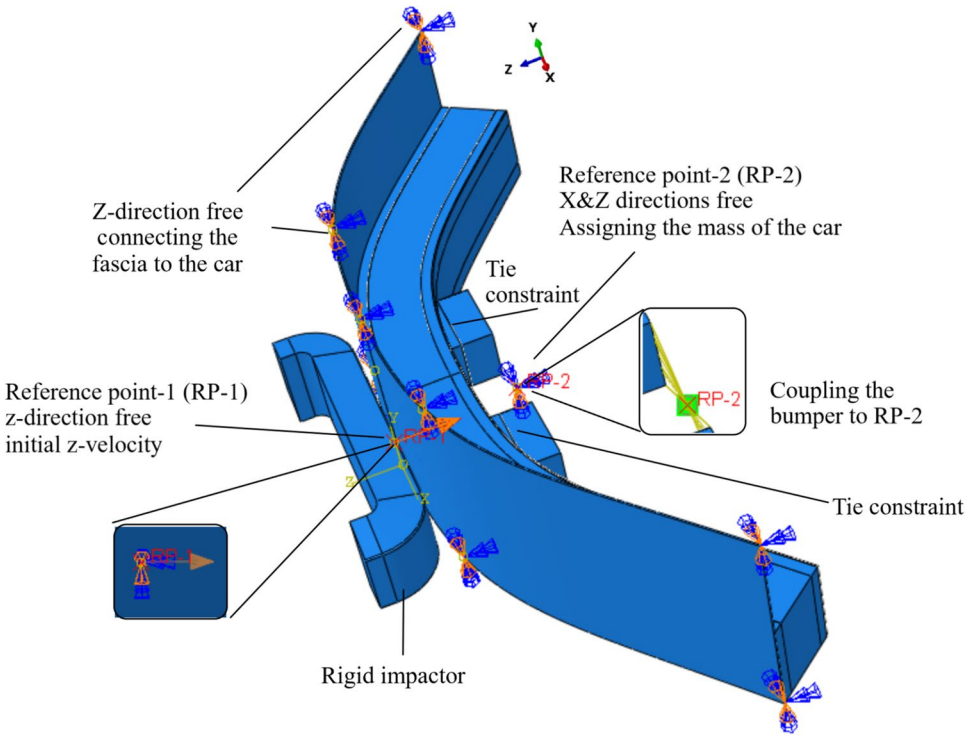

Fig. 5 Model geometry, constraints and boundary conditions for simulation

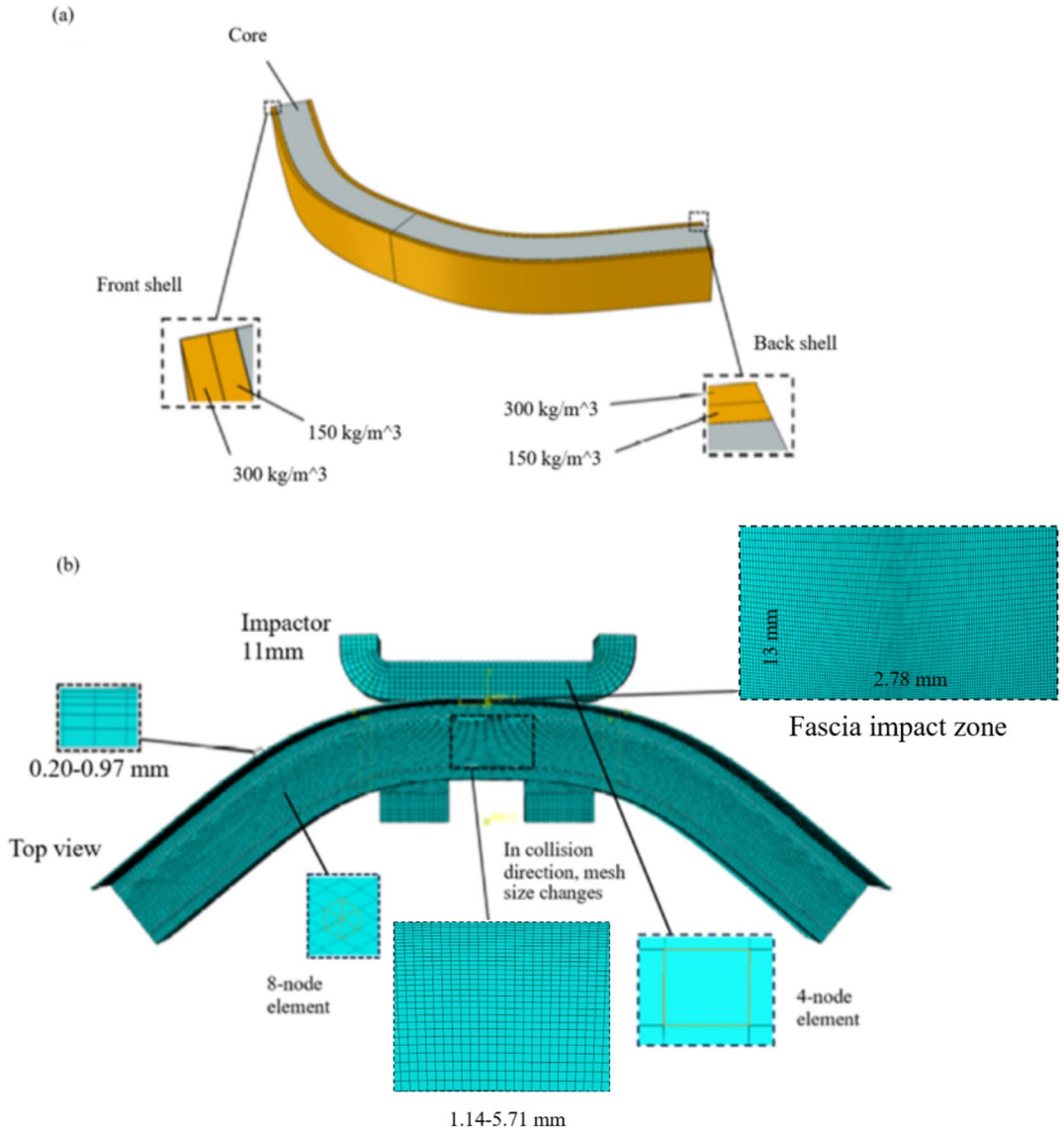

Fig. 6 The components of the bumper system and a simplified impactor: **a** showing a sandwich absorber structure with a shell thickness of 15 mm and a density of 225 kg/m^3; **b** the model mesh used in the simulation

3 Simulation procedure

3.1 Geometry description and material

Due to the complexity of the bumper system's geometry, in the present work, each component is designed separately in SOLID WORKS and imported to ABAQUS CAE for simulation. To improve the mesh accuracy and reduce computational complexity, non-essential parts such as the sharp corners and lights are removed, and minor simplifications are made in other areas. Figure 3 illustrates the bumper system and its components before and after the simplification process. The elastoplastic model is used to define the materials and behavior of the fascia, bumper beam, and separators, while the crushable foam model is used to define the absorber's behavior. Originally made of expanded polypropylene (EPP) foam, this absorber is a monolithic polymer structure absorber found in most car bumpers. Table 1 presents the thickness of each component of the bumper system. The fascia is manufactured using high-density polyethylene (HDPE), while the bumper beam and spacer are made from aluminum alloy 2024-T3. The material properties of HDPE and Al2024-T3 are presented in Table 2.

For the purpose of preventing small impacts from causing significant damage to the vehicle, this research applies E.C.E Regulation No. 42 [38], which approves protective equipment and parts located on the front and rear parts of motor vehicles for low-speed collisions. Figure 4

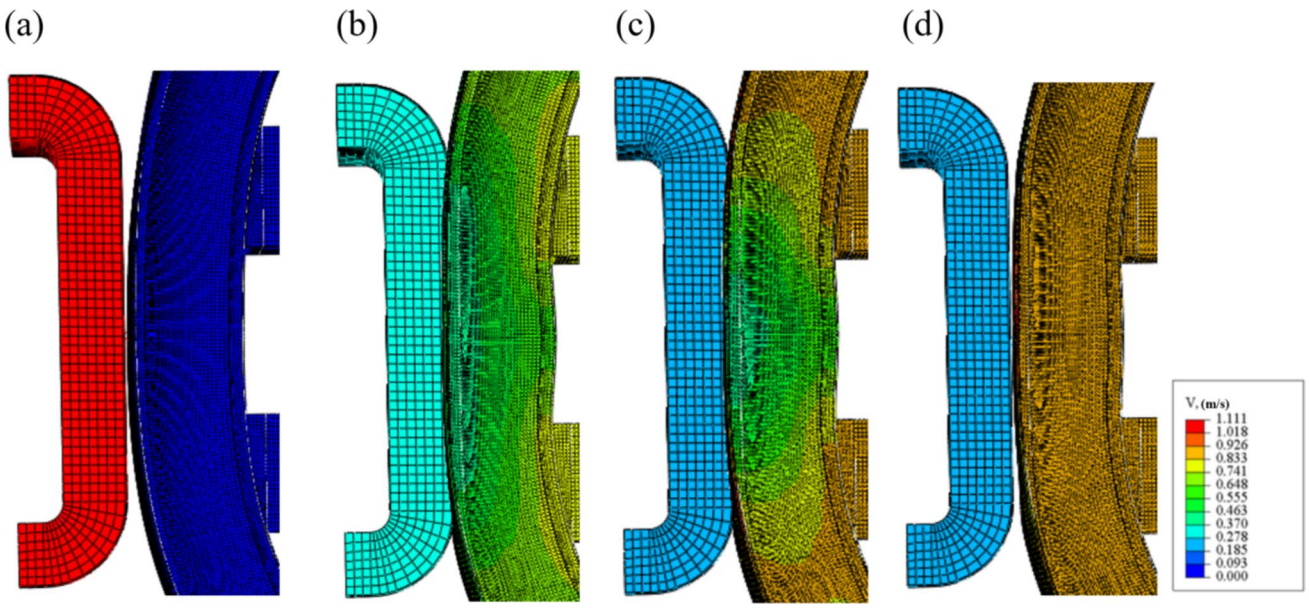

Fig. 7 Two-dimensional contour of speed of the impactor and the bumper system with sandwich structure, shell of thickness 15 mm, and density 150 kg/m^3; **a** at the beginning of the collision (t = 0 s), **b** compression phase (t = 0.034 s), **c** restitution phase (t = 0.059 s) and **d** separation moment of impactor and bumper (t = 0.078 s)

illustrates 3 views and 3D model of the impactor used in this study.

This study presents a comprehensive examination of a novel absorber design, which features a sandwich structure with a thin aluminum foam (Close cell) serving as the outer shells and the primary absorber (EPP foam) acting as the inner core, as illustrates in Fig. 6a. To investigate the effects of thickness and density parameters on the impact properties of the shell, thicknesses of 15, 20 and 25 mm and densities of 150 and 300 kg/m^3 are considered for the shell. The base metal of the foam has a density of ρ_a=2643.22 kg/m^3. Table 3 presents the properties of both aluminum foams and EPP foam.

This research investigates a unique case where the absorber is designed with a sandwich structure. Specifically, half of the absorber shell is constructed from an aluminum foam of density 150 kg/m^3, while the other half is made of foam of density 300 kg/m^3. The unique structure of this absorber is thoroughly examined and compared to other absorber models. This study model of a sandwich absorber with a shell density of 225 kg/m^3 is shown in Fig. 6a. Table 4 provides a concise summary of the different absorber models investigated.

3.2 Mesh, boundary conditions and interactions

The bumper system's main components are modeled as 3D deformable elements. The impactor is modelled as a shell in SOLID WORKS, and a rigid constraint is applied to it in ABAQUS, since the impactor is non-deformable. Following the E.C.E-R042 standard, partitioning is performed based on the components position relative to the impact zone such that the element size is reduced in areas near the contact zone to improve the computational efficiency. A mesh study is conducted and is presented in Appendix A to determine the appropriate element size. The bumper system components are modeled using 3D hexahedral elements with reduced integration (8 nodes), while the impactor is modeled with quadrilateral elements (4 nodes).

Vehicles must be stationary and unrestrained for crash simulations according to E.C.E-R042. The rigid impactor used in the simulation has a mass equivalent to that of an unmanned vehicle. At the beginning of the test, the impactor collides the stationary vehicle along the normal direction at a speed of 4 km/h [38]. After modeling the car bumper, the car mass of 1300 kg is assigned to a reference point-2 coupled to the bumper system. The separators and bumper beams are permanently connected through tie constraints. It is ensured that the constraint between the absorber shells and the core is defined to form an absorber sandwich structure so as not to be separated from each other (Fig. 5). A dynamic/Explicit solver for the analysis where the simulation duration for this complete collision test from making to ceasing contact is 0.13 s.

For all interactions between contacting surfaces including the bumper system components and impactor and fascia, explicit surface-to-surface contact is used. A "hard" contact model is employed in the normal direction, while a penalty with a coefficient of friction (COF) of 0.3 is used for tangential directions. In hard contact, when 2 objects touch each other,

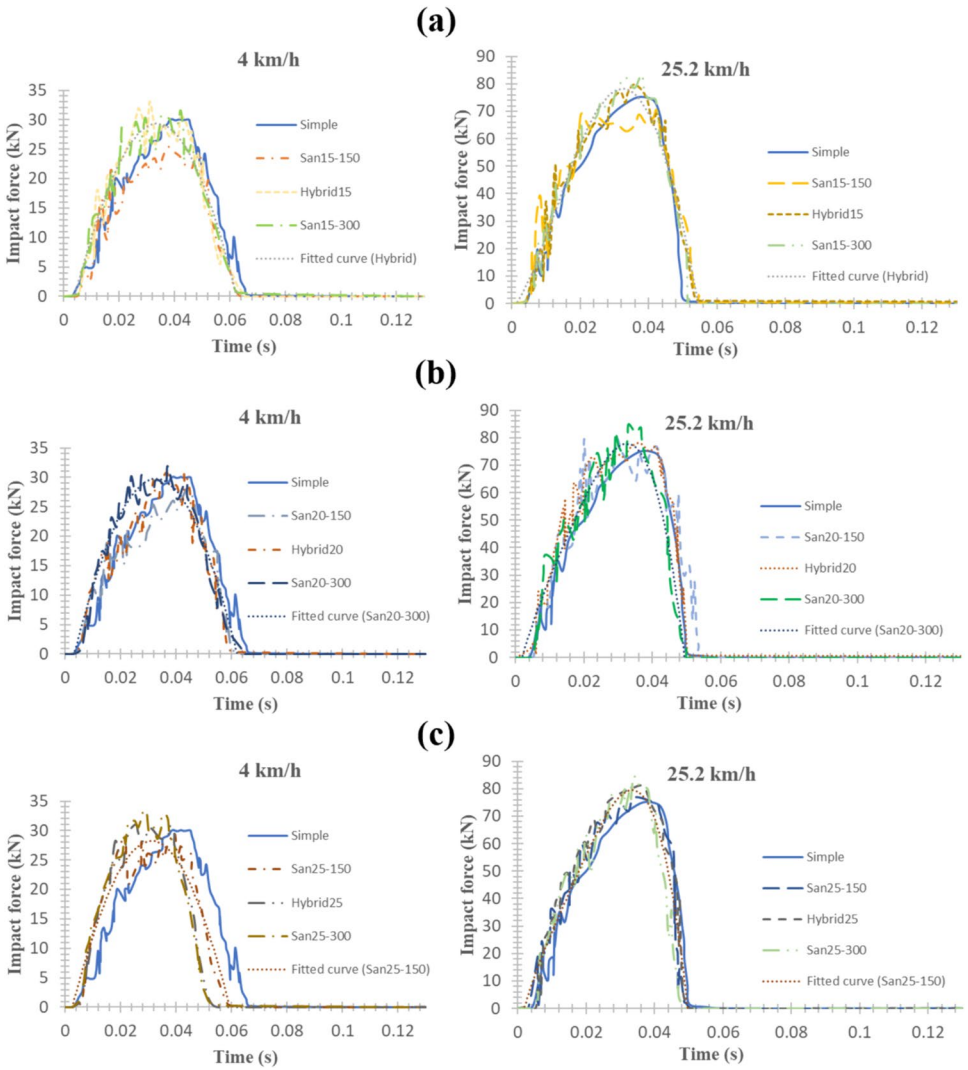

Fig. 8 Impact force changes during a collision for a simple absorber and a sandwich structure with different shell thicknesses. The shell thicknesses considered are *tsc* = 0.15, 0.20, and 0.25, displayed in parts **a**, **b**, and **c**, respectively

Table 5 Equations of the fitted curves on the collision force–time data along with the coefficient of determination (4 km/h)

Polynomial function	$F_{imp} = at^4 + bt^3 + ct^2 + dt + e$					
Model	a	b	c	d	e	Coef. of determination (R^2)
Simple	6e + 9	− 1e + 9	4e + 7	675,123	− 2567.60	0.98
San15-150	6e + 9	− 1e + 9	4e + 7	520,599	− 1489.60	0.95
Hybrid15	2e + 10	− 3e + 9	9e + 7	273,662	− 717.66	0.96
San15-300	8e + 9	− 1e + 9	3e + 7	1,000,000	− 2867.90	0.97
San20-150	8e + 8	8e + 6	− 3e + 7	2,000,000	− 5442.90	0.83
Hybrid20	6e + 9	− 1e + 9	3e + 7	830,721	− 1990.80	0.94
San20-300	3e + 9	− 3e + 8	− 3e + 7	2,000,000	− 6559.40	0.92
San25-150	3e + 9	− 4e + 8	− 2e + 7	2,000,000	− 5079.20	0.93
Hybrid25	4e + 9	− 5e + 8	− 1e + 7	2,000,000	− 6064.70	0.95
San25-300	2e + 9	− 6e + 7	− 4e + 7	3,000,000	− 7752.90	0.93

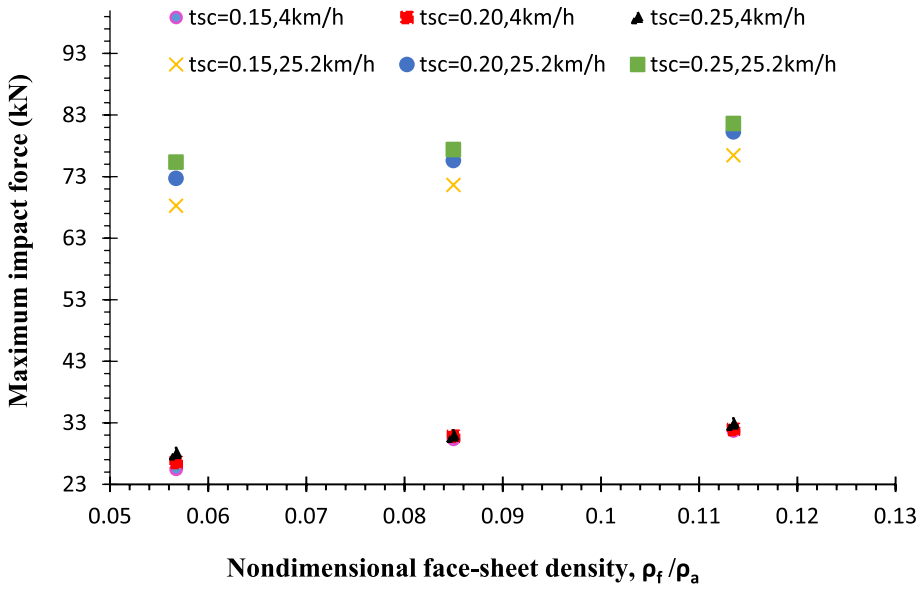

Fig. 9 Effects of the density and thickness of the absorber shell with a sandwich structure on the maximum impact force

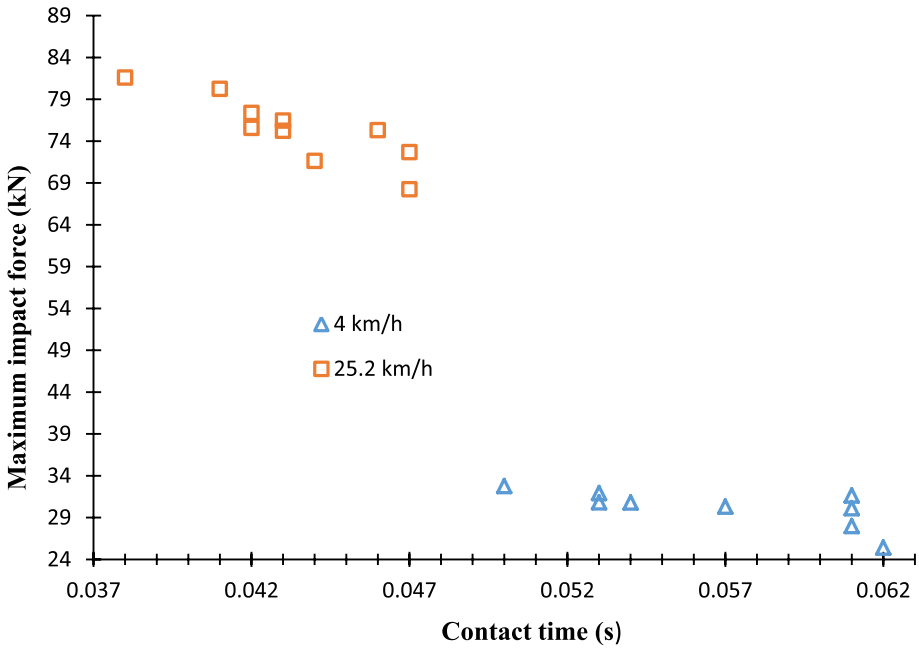

Fig. 10 Variations of maximum impact force and contact time during an impact test of different absorbers

pressure is created between the 2 objects and increases as they penetrate into each other. Thus, when the pressure becomes zero, the surfaces separate from each other (Fig. 6).

4 Results and discussion

The bumper system is at rest while the impactor moves towards it at a constant speed of 4 km/h in accordance with established standards (Fig. 7a). Upon collision, the bumper enters the compression phase, which occurs within the time interval ($0 \le t \le t_c$). During this phase, all parts of the bumper are compressed, and part of the collision energy is absorbed by the absorber and the bumper beam (Fig. 7b). The maximum compression between the bumper and the impactor occurs at t_c. Then, in the restitution phase ($0 \le t \le t_f$), the unloading process starts and continues till separation at t_f, where contact between the bumper and impactor ceases (Fig. 7c, d).

Equation (10) defines a dimensionless parameter as the ratio of the shell thickness to the absorber core thickness.

$$tsc = \frac{t_{shell}}{t_{core}}; tsc \ge 0. \tag{21}$$

4.1 Effects of the thickness and density of the absorber shell on the impact force and contact time

The impact force variations are initially examined for the case where the bumper system is combined with a simple absorber, followed by different independent variables such as density and thickness of the absorber shell. As illustrated in Fig. 8, the collision enters the compression phase immediately after impact, with the impact force rapidly increasing from zero to several kilo Newtons. Once the maximum impact force is reached, the collision transitions into the restitution phase, which starts from the peak compression point. It is a widely observed phenomenon that force–time diagrams of collisions exhibit significant force changes in a very brief period, which is one of the primary characteristics of the diagram.

The behavior of collision force data points over time can be approximated using different mathematical functions. In this study, a fourth-degree polynomial is employed to describe the changes in impact force with time, with complementary details provided in Table 5.

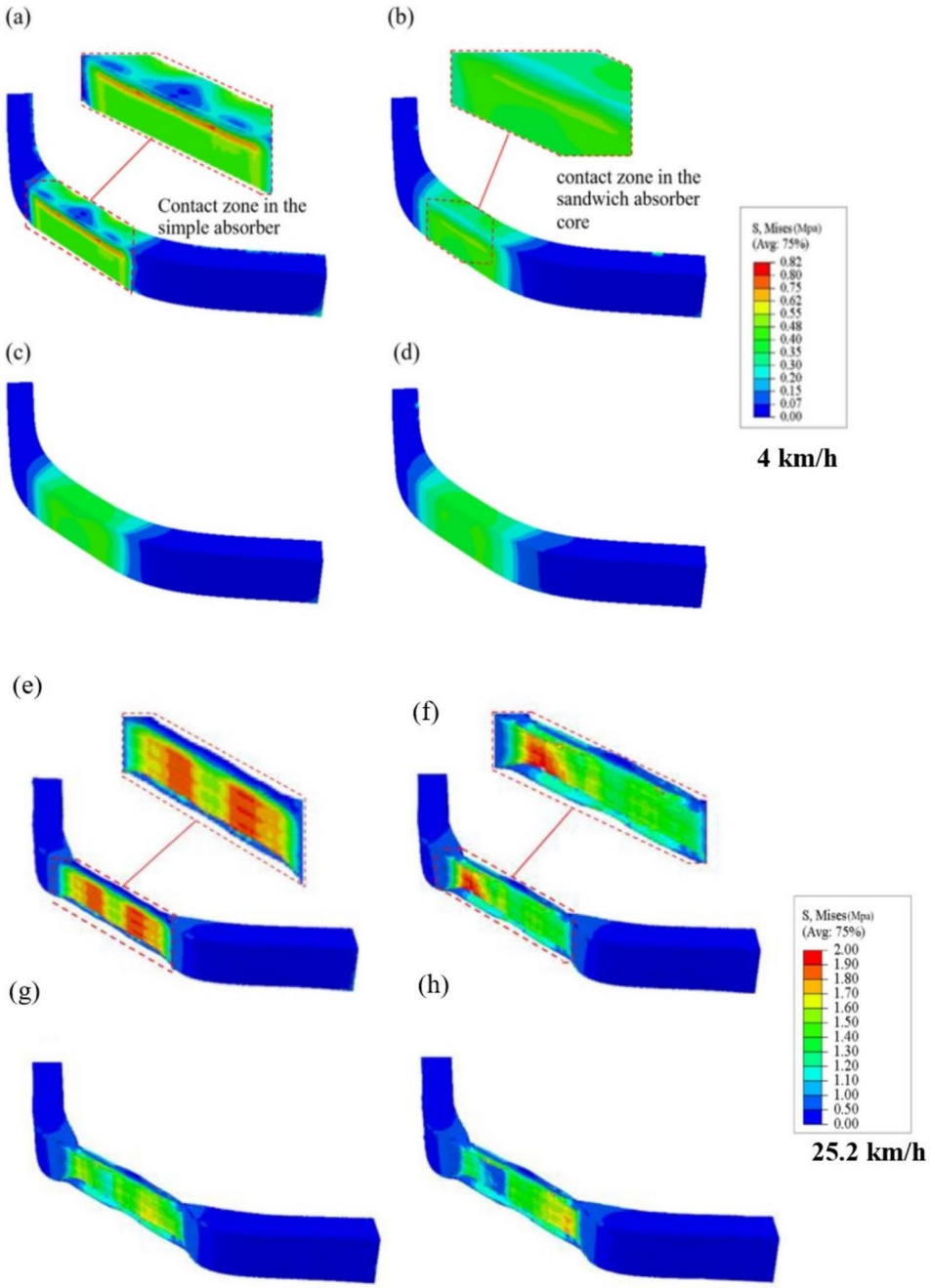

Fig. 11 The 3D contour of von Mises stress for the absorber core with a thickness of 25 mm ($tsc = 0.25$) at t_c, including 4 different models. **a**, **e** the basic model without a sandwich structure (Simple), **b**, **f** the absorber core with a shell density of 150 kg/m^3, **c**, **g** the absorber core with a hybrid structure, and **d** the absorber core with a shell density of 300 kg/m^3

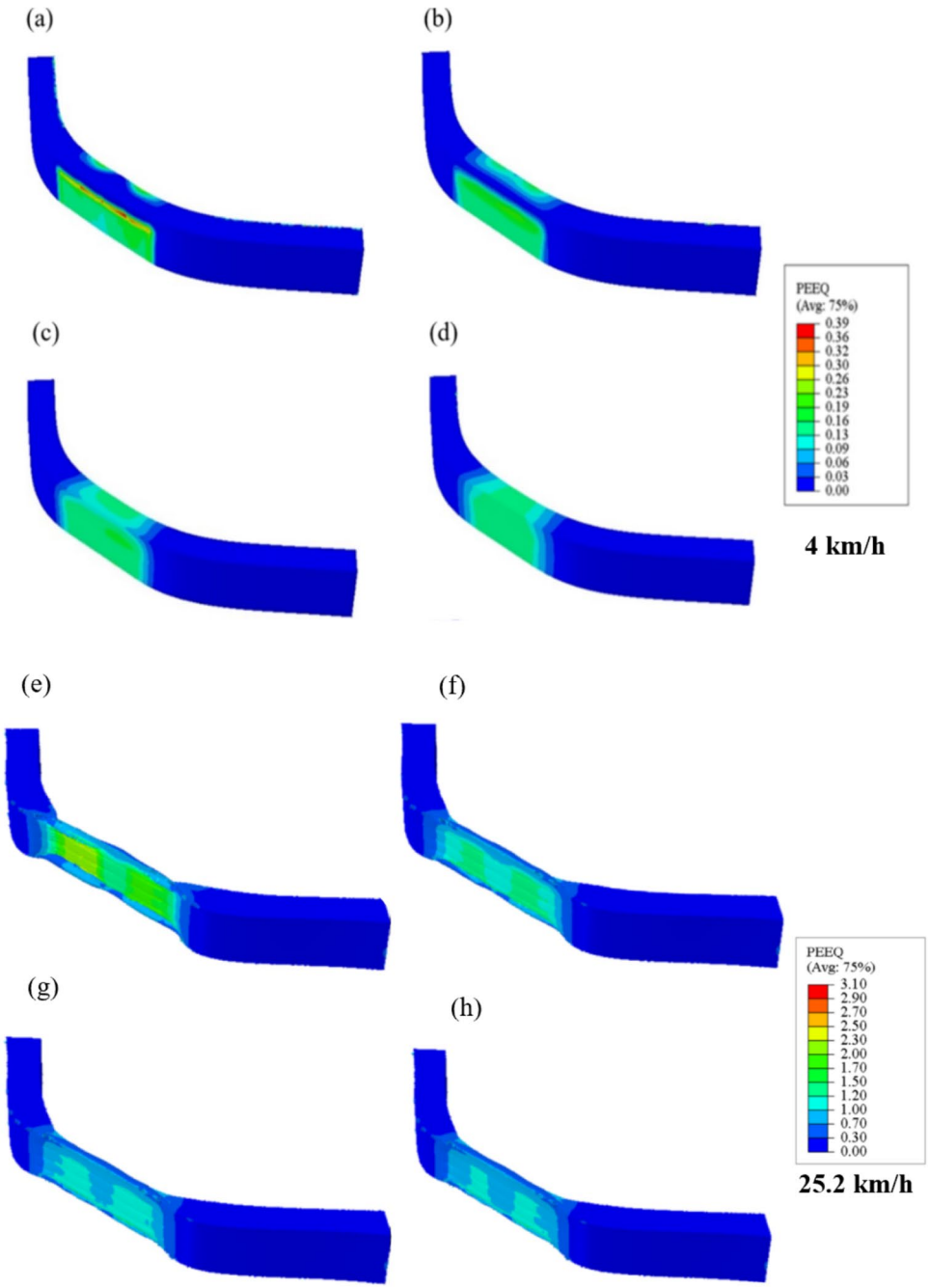

Fig. 12 The 3D contour of equivalent plastic strain for the absorber core with a thickness of 25 mm ($tsc = 0.25$) at separation; **a**, **e** basic model without sandwich structure (Simple), **b**, **f** absorber core (shell density equal to 150 kg/m^3), **c**, **g** absorber core (Hybrid) and **d**, **h** absorber core (the density of the shell is equal to 300 kg/m^3)

The maximum force applied to the simple absorber is 30.1 kN. The results are analyzed and compared with new test conditions. Figure 9 shows a 16% reduction in the maximum impact force for a 15 mm thick shell absorber, compared to the simple absorber. Hybrid15 has a maximum impact force of 30.3 kN, which is not s different from the simple absorber. A 15 mm thick shell of density 300 kg/m^3 results in a 5% increase in the maximum impact force, being 31.6 kN. Similar analyses are conducted for 2 other thicknesses. In general, based on the findings illustrated in Fig. 9, it can be inferred that the maximum impact force for shells of same thickness rises as the shell density increases. Furthermore, maintaining the density constant, by increasing the shell thickness, the maximum impact force increases. However, the growth rate of the impact force by shell thickness is slower than that experienced for the density increase.

In general, it can be evaluated as follows that a comparative analysis is conducted between the maximum impact forces obtained with simple and sandwich absorbers. In the case of a 15 mm shell thickness and a density 150 (San 15-150), the maximum impact force exhibits a significant 16% decrease compared to the simple absorber

Table 6 Improvement percentages of the absorber core compared to the simple absorber based on von Mises yielding criterion and equivalent plastic strain

Model	Improvement based on von Mises yielding criterion (%)		Improvement based on equivalent plastic strain (%)	
	4 km/h	25.2 km/h	4 km/h	25.2 km/h
San15-150	15.9	5.2	28.2	27.2
Hybrid15	38.2	17.1	31.7	33.6
San15-300	43.3	19.5	38.7	45.7
San20-150	31.6	11.4	31.9	35.9
Hybrid20	44.0	19.1	34.7	47.5
San20-300	**47.2**	22.2	40.4	54.5
San25-150	37.7	13.9	49.6	42.5
Hybrid25	46.3	21.8	57.1	54.3
San25-300	45.5	**23.1**	**62.5**	**61.1**

The Maximum values are underlined

configuration. Furthermore, as the shell density increases, the impact force also intensifies. However, for a 25 mm thickness and a density of 300 (San 25-300), the maximum impact force experiences a slight 5% increase compared to the simple case. These findings underscore the presence of a density threshold for the absorber sandwich shell, indicating the importance of selecting an optimal range based on the core's density and thickness.

To ensure accuracy, the simulations are repeated with the impact velocity of 25.2 km/h. The maximum impact force recorded at this speed is 75.2 kN. As shown in Fig. 9, the trend of the maximum impact force for different states of the sandwich absorber at this speed is similar to that at 4 km/h. Overall, the results in Fig. 9 indicate that at both speeds, the maximum collision force increases as the density increases while keep the shell thickness constant. Additionally, at a constant density, the maximum impact force shows a consistent upward trend by increasing thickness. However, the increase rate by increasing thickness is lower than that corresponding to the density.

By analyzing the contact time between the colliding objects in the impact force–time curve (Fig. 8), it is apparent that there is a slight temporal difference between the compression and restitution phases. Both phases duration can be derived from the total collision time (Eq. (22)). As expected, the contact time is directly proportional to the objects' mass and changes in velocity during the collision, while inversely related to the collision force in the normal direction due to the law of conservation of momentum (Eq. (22)).

$$t_{cont} = \int_{V1}^{V2} \frac{MdV}{F_{imp}(V)}, \tag{22}$$

$$t_{cont} = t_{comp} + t_{rest}. \tag{23}$$

It is noteworthy that thickness and density of the absorber shells are factors affecting the absorber mass. Due to the presence of aluminum foam shells, the absorber mass is larger in all cases compared to the simple case. Thus, the absorber mass can be introduced as one of the effective factors in determining the contact time. However, note that the shell mass is negligible in comparison to that of the car. The study finds that variations in effective mass do not significantly affect the contact time, but such change can influence the maximum impact force.

Figure 10 shows that changes in the thickness and density of the sandwich absorber shell affect the contact time. Furthermore, it can be observed that the contact time increases as the impact force decreases.

Through the incorporation of aluminum foam shells and modifications to the absorber structure, the mass of the system increases, resulting in alterations to the normal compliance within the contact area between the absorber and other bumper components. Consequently, these changes influence the maximum impact force experienced during collisions. The absorber mass, as well as the overall mass of the bumper system, plays a role in determining the contact time, following the law of conservation of momentum. However, a noticeable trend emerges during the study, indicating that the maximum impact force has a more significant impact compared to other parameters. This is evidenced by the increasing contact time alongside the decrease in maximum impact force, despite a slight increase in absorber mass.

By comparing the contact times at the 2 different speeds, it is evident that an increase in collision speed results in a decrease in contact time. At speed of 25.2 km/h, in all conditions, the contact time is consistently shorter than that at speed of 4 km/h.

4.2 Analysis of maximum von Mises stress and equivalent plastic strain for absorbers with different shell thickness and density

It is crucial to study the performance and durability of a bumper system with a modified absorber. To achieve this goal, simulations are conducted on the bumper system, and its performance is studied at t_c which represents the largest compression. The von Mises stress contour is considered for this purpose. Equivalent plastic strain (PEEQ) is a scalar positive quantity. It indicates the degree of plasticity of a structure at all its points. An analysis of the PEEQ at

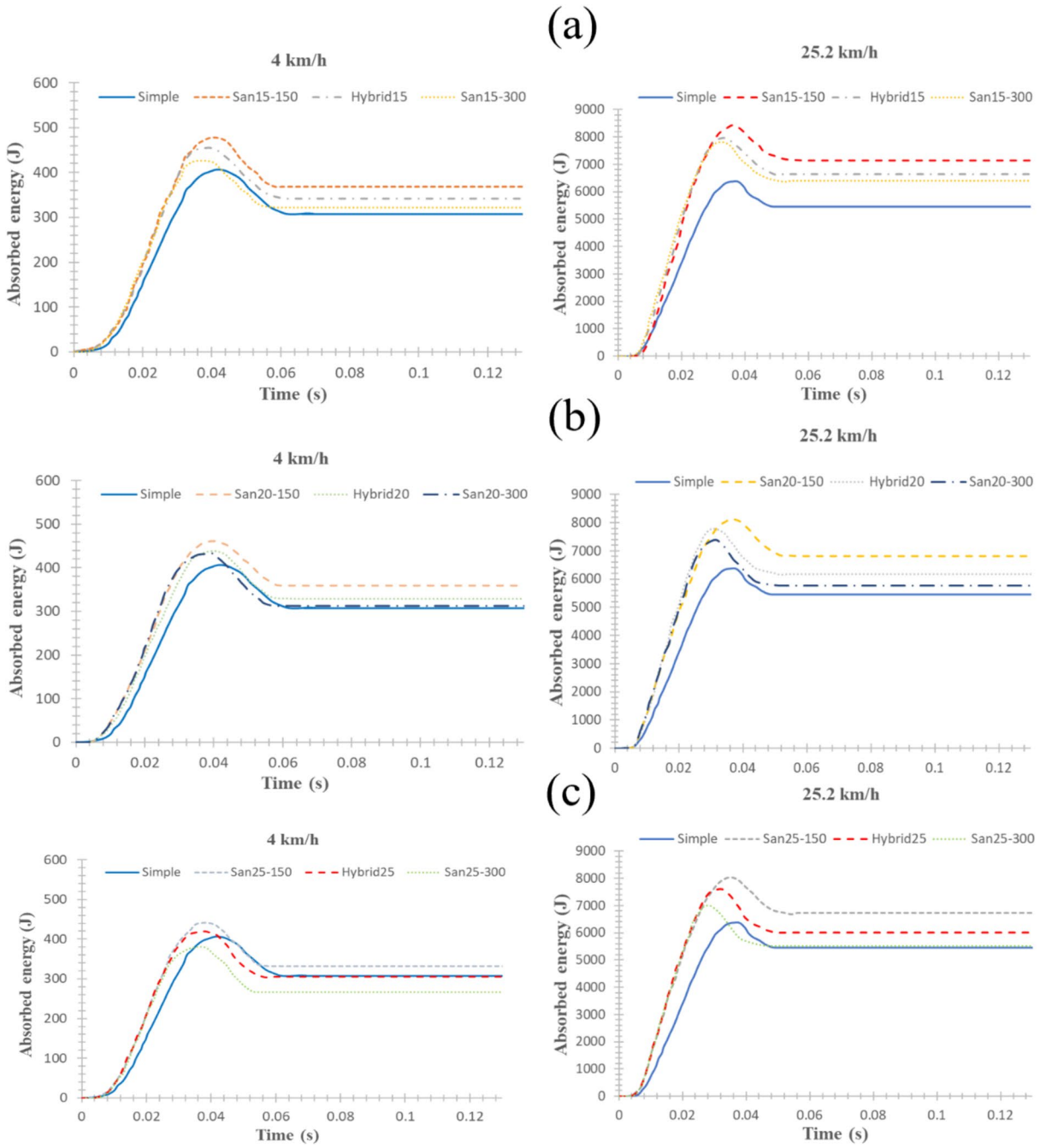

Fig. 13 Comparing the energy-time diagrams of the simple model with those of the sandwich cases with **a** $tsc = 0.15$, **b** $tsc = 0.20$ and **c** $tsc = 0.25$

the point of separation is conducted to determine the areas that experience plastic deformation. The absorber core was used as a sample to enable a logical comparison between all cases.

Figures 11 and 12 show that the von Mises stress and the equivalent plastic strain of the absorber decrease proportionally with the absorber shell density and that the sandwich absorber outperforms the simple absorber. The superior mechanical properties of aluminum foam contribute to the enhanced performance of the sandwich absorbers. The maximum equivalent plastic strain for the simple absorber under collision velocities 4 and 25.2 km/h are 0.389 and 3.10, respectively, which are higher than that of the sandwich models, while the maximum von Mises stress are 0.82 and 2 MPa, respectively, which are also higher than that of the sandwich absorber core. These results demonstrate that

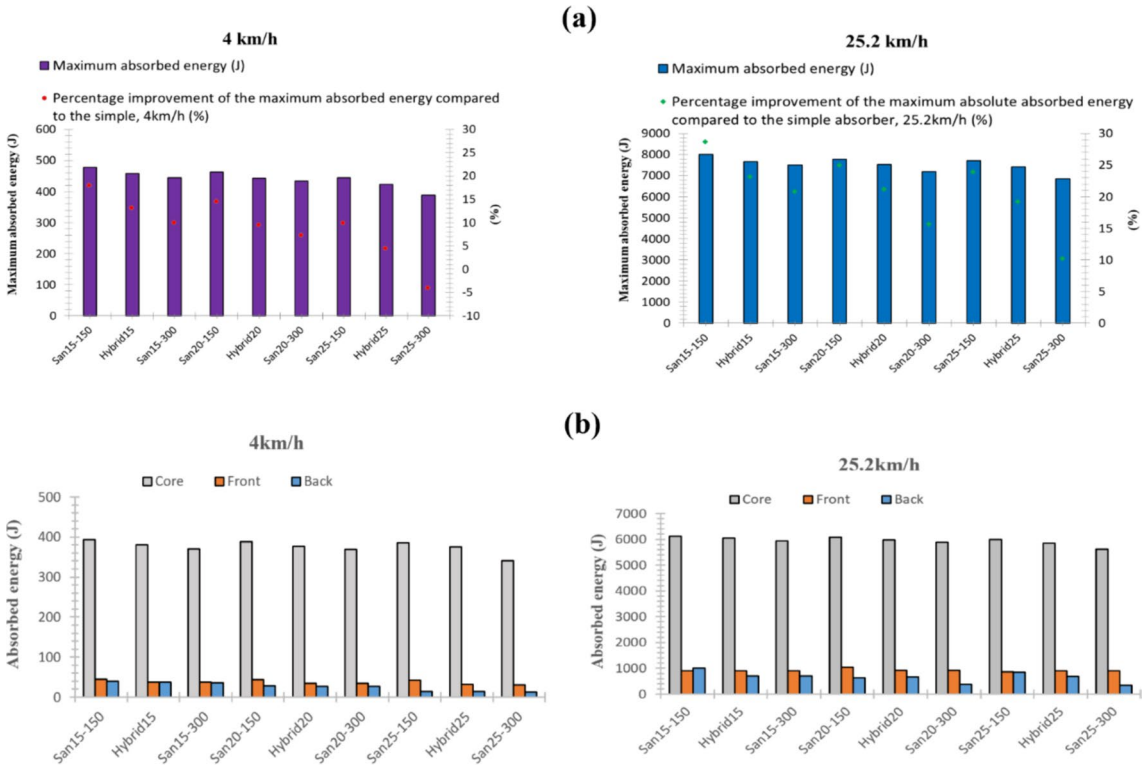

Fig. 14 Comparing the sandwich absorber's energy absorption performance of different studied models: **a** maximum absorbed energy, and **b** distribution of absorbed energy among the absorber components

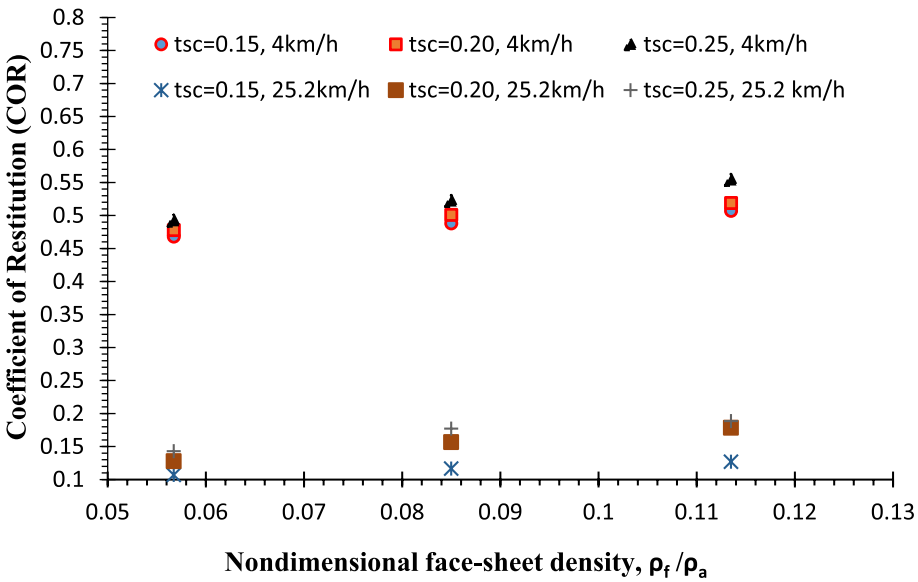

Fig. 15 The coefficient of restitution of the absorber versus the shell density for different thicknesses

the sandwich absorber core is more durable and can withstand deformation better than the simple absorber model. In this section, apart from the comprehensive analysis of the maximum von Mises stress and maximum equivalent plastic strain, various models, as illustrated in Fig. 11, showcase the von Mises stress contour for both a simple absorber and a sandwich absorber core with a 25 mm thickness at different densities during the peak compression time (t_c).

Additionally, Fig. 12 provides the contour of equivalent plastic strain at the same thickness for the sandwich absorber during the separation event.

Table 6 presents the percentage reduction in both maximum von Mises stress and maximum equivalent plastic strain within the cores of the sandwich absorber in comparison to the simple absorber. Notably, at a thickness of 15 mm, an increase in shell density resultes in a reduction of maximum von Mises stress compared to the simple case, a consistent trend for higher thicknesses (20 and 25 mm). This reduction pattern continues as shell density ranges from 150 kg/m^3 to 300 kg/m^3, with the percentage difference amplifying.

An interesting observation is the peak difference in maximum equivalent plastic strain occurring at a thickness of 25 mm and a density of 300 kg/m^3 (San 250-300) at 62.5%. Conversely, the maximum reduction in von Mises stress compared to the simple absorber is noted at a thickness of 20 mm and a density of 300 kg/m^3 (San 20-300) with a 47.2% decrease. However, at a density of 300 kg/m^3 and a thickness of 25 mm, this reduction is 45.5%, not significantly divergent from San 25-300. This consistent pattern was observed for both the von Mises yield criterion and the equivalent plastic strain.

The maximum von Mises stress in 4 km/h experienced by the core during maximum compression is observed to decrease within a range (15.9%–47.2%) in all cases, compared to the simple absorber configuration. Additionally, the maximum equivalent plastic strain in the absorber core during the separation phase exhibits a reduction between (28.2%, 62.5%) across all cases. These reductions are consistent with the increase in absorber shell density while maintaining the same thickness. Notably, it is observed that higher densities in the absorber shell result in decreased maximum von Mises stress and maximum equivalent plastic strain within the absorber core.

Table 7 Parameters and related levels

Parameter	Level (unit)
Thickness	15 (mm)
	20 (mm)
	25 (mm)
Density	150 (kg/m^3)
	225 (kg/m^3)
	300 (kg/m^3)

Table 8 Taguchi orthogonal array (L9)

Simulation	Density (kg/m^3)	Thickness (mm)	F_{max} (kN)	Max. von Mises (Mpa)	Max. equivalent plastic strain	Energy (J)	COR
1	150	15	25.42	0.71	0.30	477.42	0.47
2	150	20	30.30	0.59	0.29	463.32	0.48
3	150	25	31.64	0.57	0.28	444.52	0.49
4	225	15	26.55	0.62	0.29	457.91	0.49
5	225	20	30.80	0.56	0.28	442.95	0.50
6	225	25	31.92	0.55	0.27	422.87	0.52
7	300	15	27.98	0.59	0.26	445.23	0.51
8	300	20	30.82	0.56	0.25	434.12	0.52
9	300	25	32.77	0.56	0.24	388.39	0.55

Table 9 Grey relational generation

Simulation	Grey relational				
	F_{max} (kN)	Max. von Mises (Mpa)	Max. equivalent plastic strain	Energy (J)	COR
1	1	0	0	1	0
2	0.336054	0.750	0.166667	0.841610	0.116279
3	0.153741	0.875	0.333333	0.630427	0.279070
4	0.846259	0.5625	0.166667	0.780808	0.232558
5	0.268027	0.9375	0.333333	0.612848	0.383721
6	0.115646	1	0.50	0.387208	0.627907
7	0.651701	0.750	0.666667	0.638447	0.453488
8	0.265306	0.9375	0.833333	0.513586	0.593023
9	0	0.9375	1	0	1

4.3 Effects of shell thickness and density on energy absorption

This section includes an analysis of the energy absorption of the bumper system's absorber. Sandwich absorber models, except for the San25-300 model, exhibit higher energy absorption compared to the simple absorber model, as shown in Fig. 13. For example, the sandwich model with a shell thickness of 15 mm and a density of 150 kg/m^3 absorbs up to 477.42 J, surpassing the maximum energy absorption of the simple model being 404.6 J. Figure 14a provides a

Table 10 Grey relational coefficient and Grey relational grade

Simulation	Grey relational coefficient					
	F_{max} (kN)	Max. von Mises (Mpa)	Max. equivalent plastic strain	Energy (J)	COR	Grey relational grade
1	1	0.3333	0.3333	1	0.3333	0.60
2	0.4296	0.6667	0.3750	0.7594	0.3613	0.5184
3	0.3714	0.80	0.4286	0.5750	0.4095	0.5169
4	0.7648	0.5333	0.3750	0.6952	0.3945	0.5526
5	0.4059	0.8889	0.4286	0.5636	0.4479	0.5470
6	0.3612	1	0.50	0.4493	0.5733	0.5768
7	0.5894	0.6667	0.60	0.5803	0.4778	0.5828
8	0.4050	0.8889	0.750	0.5069	0.5513	0.6204
9	0.3333	0.8889	1	0.3333	1	0.7111

Table 11 Average gray relation grade (GRG) based on the parameter levels

Level	Density (kg/m^3)	Thickness (mm)
1	0.5451 (150)	0.5785 (15)
2	0.5293 (225)	0.5619 (20)
3	**0.6381 (300)**	**0.6016 (25)**

The maximum values are underlined

detailed analysis of the maximum energy absorption for the considered models. Also, at the speed of 25.2 km/h, the maximum absolute energy absorption by the simple absorber is 6218 J, and the trend is similar to that of the speed of 4 km/h for different models. However, as could be predicted, the absolute values of energy absorption are significantly larger compared to the collision at the speed of 4 km/h.

Hassanli and Paydar [26] found that under uniaxial compressive loading, energy absorption in aluminum foams decreased as density increased. The same trend was observed in this research when the shell thickness was constant, and the density increased from 150 to 300 kg/m^3.

Knowledge of partial energy absorbed by different components of the sandwich absorber is important in designing bumper absorbers. Figure 14b shows that, in all cases, the core absorbs 70%–90% of the impact energy, while the front and back shells absorb less.

In summary, it can be said, the investigation of energy absorption in sandwich structure absorbers highlights an overall improvement in energy absorption, with the exception of the San25-300 case when compared to the simple absorber configuration. When the density is increased while maintaining a constant thickness, there is a decrease in the total energy absorption (E). This observation is evident in the San25-300 case, where the energy absorption is lower compared to the simple case. These findings emphasize the importance of selecting an appropriate density range for the absorber shell, as there exists a specific interval that optimizes energy absorption performance.

In the absorber with a sandwich structure, comprising a core and shell with varying densities and thicknesses, both components contribute significantly to energy absorption in a similar ratio. Roughly, 70%–90% of energy is absorbed by the core, with the remaining portion attributed to the shells. This suggests that metal foams, due to their mechanical properties, exhibit lower energy absorption compared to polymer foams. While the amount of energy absorption in sandwich absorber cores is observed to be lower than in the simple case, the overall energy absorption increases due to the additional energy absorption provided by the shells.

Equation (24) states square of the coefficient of restitution (COR), e_*, as the negative ratio of the elastic strain energy released during restitution (E_r) to the internal energy of deformation absorbed during compression (E_c), [30].

$$e_*^2 = -\frac{E_r}{E_c}; 0 \le e_* \le 1. \tag{24}$$

Figure 15 illustrates that the coefficient of restitution remains within a short range, with deviations below 10% from the COR of the simple absorber being 0.50. It can be inferred that increasing the shell thickness leads to larger CORs, considering the same density. Additionally, when the velocity and thickness of the shell remain constant, an increase in density results in a slight increase in the COR, In other words, Modifications in shell density, thickness, and absorber structure don't exert a substantial influence on the coefficient of restitution (COR) of the absorber, as the observed changes remain below 10%. However, it is worth noting that as the density of the shell increases, the COR of the absorber demonstrates a gradual upward trend, albeit with a mild slope.

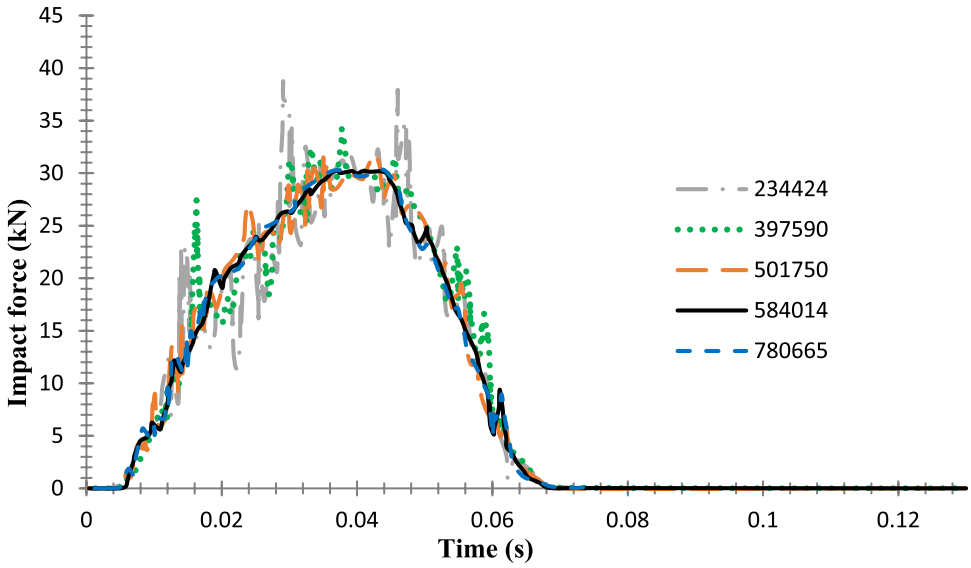

Fig. 16 1 The force–time curve of 5 cases with different number of elements considered in the mesh study

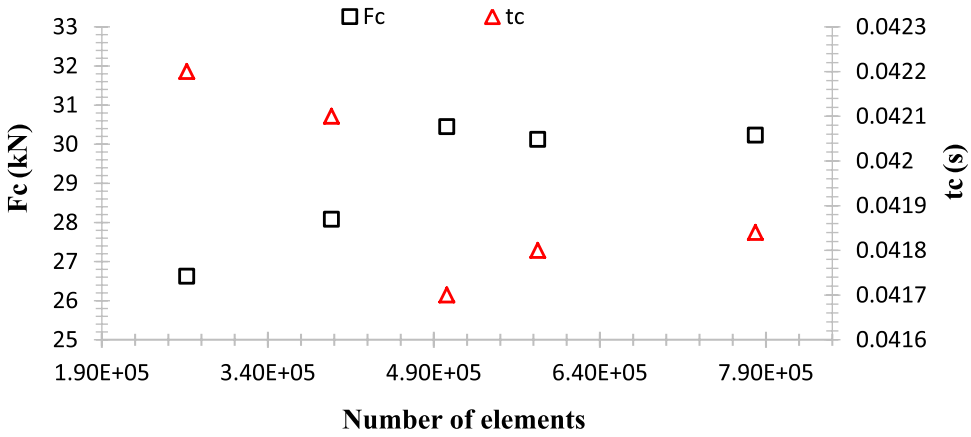

Fig. 17 Studying the mesh convergence examining maximum impact force (F_c) and the compression time (t_c)

Table 12 Comparison of 5 cases with different number of elements

Case	Number of 8-node elements	Number of 4-node elements	F_c (kN)	diff. (%)	t_c (s)	diff. (%)
1	233,438	986	26.6	11.6	422e − 4	0.9
2	395,786	1804	28.1	6.8	421e − 4	0.7
3	499,152	2598	30.4	1.1	417e − 4	0.2
4	**580,212**	**3802**	**30.1**	–	**418e − 4**	–
5	773,352	7313	30.2	0.3	418e − 4	~0.1

As the result of mesh study, the number of elements corresponding to the bold row was considered in the simulations

4.4 Optimization

A study was conducted to optimize several performance metrics of an absorber at 4 km/h collision speed. The aims were to reduce the maximum impact force, von Mises stress, and equivalent plastic strain, while increasing energy absorption and COR. The study focused on 2 controlling parameters: density and shell thickness, each with 3 levels mentioned in Table 7. The Taguchi method was employed to minimize the number of calculations

by analyzing the simultaneous effects of the considered parameters.

Finally, analysis of variance (ANOVA) was used to assess the influence of these parameters on the performance metrics. Table 8 presents the Taguchi orthogonal array and the related results. The values of the considered parameters are normalized using Eqs. (16) and (17). It is noteworthy that for impact force, von Mises stress, and equivalent plastic strain, lower values and for energy absorption and COR, upper values are preferable (Table 9).

In the next step, using relations (18) and (19) with $\zeta = 0.5$ and $x_0=1$, GRCs for the parameters are calculated, and GRGs are determined using relation (9) (Table 10). Finally, the average GRGs is calculated based on parameter levels, as shown in Table 11.

From Table 11, it is found that a density of 300 kg/m^3 and a thickness of 25 mm scored the highest, indicating the most optimal combination among the examined cases. However, since the maximum impact force exceeded the that of the simple absorber at a density of 300 kg/m^3, the density of 150 kg/m^3 is selected as the optimal value.

5 Conclusion

In this study the 3D finite element method (FEM) is used to investigate the behavior of car front bumper absorbers with a sandwich structure containing aluminum foam during low-speed collisions. The effects of thickness and density of the outer thin shells on the absorber's performance during impact tests is examined using a standard impactor. This research assesses effectiveness of the new absorber of densities 150, 225, and 300 kg/m3 and thicknesses 15, 20, and 25 mm, while comparing with the primary model of the absorber containing a polymer integrated structure. The analysis includes factors such as the maximum impact force, von Mises stress, equivalent plastic strain, and contact time, absorbed energy, and the coefficient of restitution of the absorber. The important results are summarized as follows:

1) Comparative analysis reveals that increasing density in sandwich absorbers affect impact forces, with a 16% decrease for San 15-150 and a 5% increase for San 25-300, emphasizing the importance of selecting optimal density and thickness.
2) Maximum von-Mises stress and equivalent plastic strain in the absorber core decrease within a range of (15.9%–47.2%) and (28.2%–62.5%), respectively, correlating with increasing the absorber shell density while maintaining its thickness.
3) Energy absorption in sandwich absorbers is generally improved, except for San25-300, emphasizing the importance of selecting an appropriate density range for optimal performance.

Table 13 Comparison of 3 examined modes for car bumper material model

Model	Energy absorbing (J) (at 60 mm deformation)	diff. (%)	Initial peak load (kN)	diff. (%)
Experimental [32]	13.5	–	9.1	–
FEM model [32]	11.7	15.3	9.1	~0
FEM model	12.3	9.7	8.6	5.8

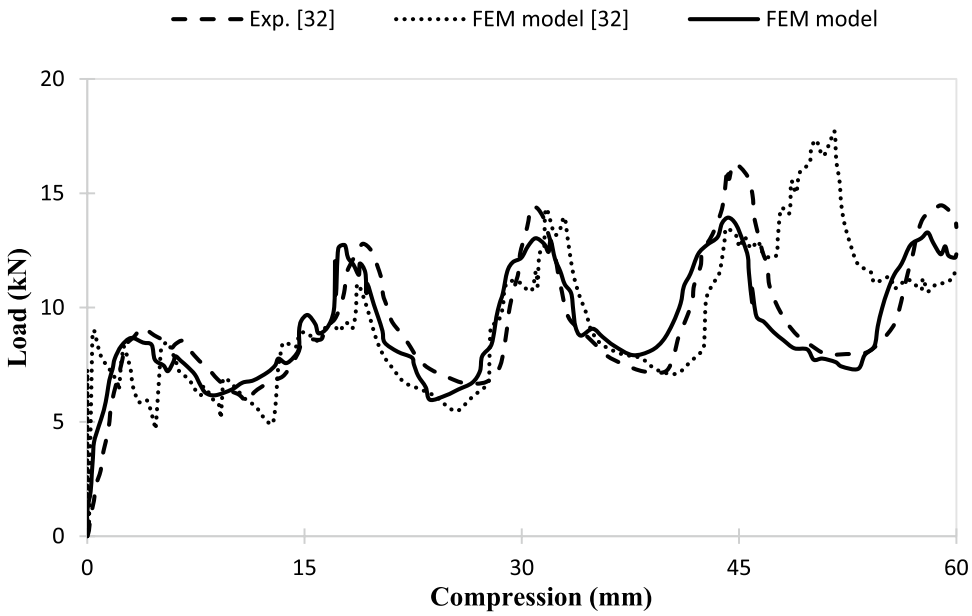

Fig. 18 A conical tube filled with foam (145 kg/m^3): a comparison of the force–displacement diagram obtained from the current study and experimental testing and FEM modeling [32]

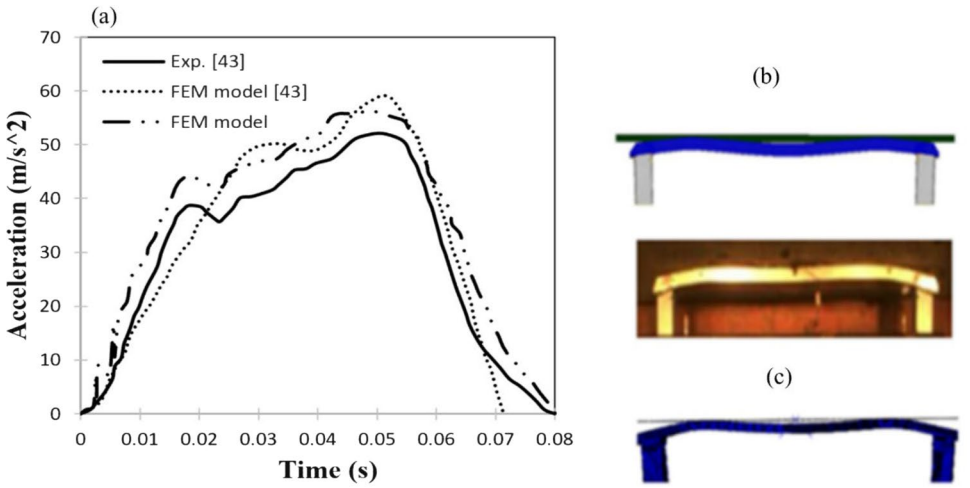

Fig. 19 **a** Acceleration data of the impactor obtained from the present FEM simulations and results of [39], **b** the reported shape of the bumper in [39], and **c** the shape obtained from the present simulation during the restitution phase

Table 14 Comparison of 3 tested bumper models during the crash test

Model	Initial peak load (kN)	diff. (%)	Second peak load (kN)	diff. (%)	End time (s)	diff. (%)
Experimental [39]	39.3	–	52.3	–	0.08	–
FEM model [39]	50.3	21.8	58.8	11	0.07	14.3
FEM model	44	10.6	55.9	6.4	0.08	~0

4) The sandwich absorber's different components contribute significantly to energy absorption, mostly attributed to the core (70%–90%). In the sandwich absorber structure, metal foams exhibit lower energy absorption than polymer foams.
5) The shell density variations significantly influenced maximum von Mises stress, maximum impact force, and maximum equivalent plastic strain, whereas change in the shell thickness did not yield significant effects. Interestingly, alterations in both density and thickness did not bring about a significant change in the coefficient of restitution (below 10%).
6) By re-examining the collision at a higher speed (25.2 km/h), it is found that aside from the expected changes in values, there is no observable change in the trend of results compared to those related to the standard speed (4 km/h). Analysis of variance is used to determine the parameters' optimal values for the absorber best performance, resulting in the absorber shell density and thickness of 150 kg/m^3 and 25 mm, respectively.

Appendix A

Mesh study

This study aims to determine the optimal number of elements for a bumper system with a simple absorber based on the force variations during impact (Fig. 16), maximum impact force, and compression time duration with different mesh sizes at a speed of 4 km/h. Five simulations with different numbers of mesh were performed.

Figure 17 shows that cases 4 and 5 converged to the same values; hence, element size of case 4 should be chosen for meshing. Table 12 presents results of the 5 simulations meshed with 2 types of elements, 4- and 8- node elements in the bumper system and impactor, respectively. This table provides the maximum impact force (F_c) and the compression time (t_c) for each model along with the differences with simulation results of the reference case 4.

Appendix B

Validation of material models of bumper components

The ability of an aluminum foam-filled conical tube in absorbing energy was validated through an axial quasi-static compression test [32]. The experiment was simulated with an explicit quasi-static scheme, using the same material properties, mesh size, and element type. A compressive deformation of 60 mm at 10 mm/min was applied to the fixed sample. The 97.5 mm long aluminum conical tube thickness was 1 mm in the upper and 0.85 mm in the

lower sections, with a diameter of 1.31 and 1.65 mm in the upper and lower sections, respectively. The foam in the aluminum shell had a density of 145 kg/m^3. To validate the FEM model of this problem, the numerical results in the current research are compared with the results obtained in [32]. In Fig. 18, the load–displacement diagram illustrates the energy absorption in each model. Notably, the crushable foam and elastoplastic model demonstrates accurate predictions for the behavior of foam and aluminum, respectively. In Fig. 18, the comparison between the simulation performed in this research and ref. [32] can be seen. Additionally, Table 13 provides a detailed comparison of the 3 models under investigation.

Appendix C

Validation of bumper modelling during impact test

The bumper system model was validated using experimental and numerical data from [39] after validating the material models of the absorber and other parts. This study evaluates the bumper system according to the IIHS standard and uses aluminum 6063-T4 and 6063-T6 in its construction, with an elastic modulus of 70 GPa, the density of 2700 kg/m^3, and Poisson's ratio of 0.3. The bumper system model is meshed with 3 mm elements.

Figure 19 illustrates the changes in the acceleration of the car's front bumper across 3 different models during the collision with an obstacle. In Fig. 19 b and c, the bumper's shape is displayed during the restitution phase. A strong agreement between the acceleration data of the results of low-speed impact test and simulation in [39] and the results of the simulation conducted in this study (Fig. 19). Notably, Table 14 presents a comparison of the reviewed models.

References

1. Mulage RB, Garje AK (2017) Crash analysis of light motor vehicle bumper system. Int J Adv Trends Eng Technol 2(2):238–242. https://doi.org/10.5281/zenodo.1123500
2. M Pasandidehpour, M Shariyat (2017) Multiobjective design optimization for crash safety of a vehicle with a viscoelastic body and wide tapered multi-cell energy absorber using DOE method. Int J Automot Eng https://doi.org/10.22068/ijae.7.3.2448
3. Natarajan N, Joshi P, Tyagi RK (2021) Design improvements of vehicle bumper for low speed impact. Mater Today Proc 38:456–465. https://doi.org/10.1016/j.matpr.2020.08.212
4. Sonawane CR, Shelar AL (2018) Strength enhancement of car front bumper for slow speed impact by FEA Method as per IIHS regulation. J Inst Eng Ser C 99(5):599–606. https://doi.org/10.1007/s40032-017-0365-y
5. Hu Y, Liu C, Zhang J, Ding G, Wu Q (2015) Research on carbon fiber-reinforced plastic bumper beam subjected to low-velocity frontal impact. Adv Mech Eng 7(6):1–15. https://doi.org/10.1177/1687814015589458
6. Wang T, Li Y (2015) Design and analysis of automotive carbon fiber composite bumper beam based on finite element analysis. Adv Mech Eng 7(6):1–12. https://doi.org/10.1177/1687814015589561
7. Shukla AK, Majumdar JD (2019) Studies on microstructure and mechanical properties of aluminium foam prepared by spray forming route. Procedia Manuf 35:861–865. https://doi.org/10.1016/j.promfg.2019.06.032
8. Ulbin M, Glodez S (2021) Fatigue analysis of closed-cell aluminium foam using different material models. Trans Nonferrous Met Soc China 31(9):2787–2796. https://doi.org/10.1016/S1003-6326(21)65693-5
9. Deshpande VS, Fleck NA (2000) Isotropic constitutive models for metallic foams. J Mech Phys Solids 48(6):1253–1283. https://doi.org/10.1016/S0022-5096(99)00082-4
10. Deshpande V, Fleck N (2001) Collapse of truss core sandwich beams in 3-point bending. Int J Solids Struct 38(36–37):6275–6305. https://doi.org/10.1016/S0020-7683(01)00103-2
11. Davoodi MM, Sapuan SM, Yunus R (2008) Conceptual design of a polymer composite automotive bumper energy absorber. Mater Des 29(7):1447–1452. https://doi.org/10.1016/j.matdes.2007.07.011
12. Davoodi MM, Sapuan SM, Ahmad D, Aidy A, Khalina A, Jonoobi M (2011) Concept selection of car bumper beam with developed hybrid bio-composite material. Mater Des 32(10):4857–4865. https://doi.org/10.1016/j.matdes.2011.06.011
13. Beyene AT, Koricho EG, Belingardi G, Martorana B (2014) Design and manufacturing issues in the development of lightweight solution for a vehicle frontal bumper. Procedia Eng 88:77–84. https://doi.org/10.1016/j.proeng.2014.11.129
14. Xiao Z, Fang J, Sun G, Li Q (2015) Crashworthiness design for functionally graded foam-filled bumper beam. Adv Eng Softw 85:81–95. https://doi.org/10.1016/j.advengsoft.2015.03.005
15. Diaz-Alvarez A, Jiao-Wang L, Feng C, Santiuste C (2020) Energy absorption and residual bending behavior of biocomposites bumper beams. Compos Struct 245:112343. https://doi.org/10.1016/j.compstruct.2020.112343
16. Archakam PK, Muthuswamy S (2021) Design and simulation of a crash energy absorption system integrated with magneto-rheological absorber. J Vib Eng Technol 9(7):1635–1656. https://doi.org/10.1007/s42417-021-00318-6
17. Wang E, Yao R, Luo Q, Li Q, Lv G, Sun G (2022) High-temperature and dynamic mechanical characterization of closed-cell aluminum foams. Int J Mech Sci 230:107548. https://doi.org/10.1016/j.ijmecsci.2022.107548
18. Hou W, Li M, Zhang X, Liu Z, Sang L (2023) Design and optimization of the bumper beam with corrugated core structure of fiber metal laminate subjected to low-velocity impact. Thin-Walled Struct 187:110746. https://doi.org/10.1016/j.tws.2023.110746
19. Lopes R et al (2023) Coach crashworthiness and failure analysis during a frontal impact. Eng Fail Anal 151:107369. https://doi.org/10.1016/j.engfailanal.2023.107369
20. Liu E et al (2024) Mechanical enhancement of aluminum foam via in situ interfacial bonding. Int J Mech Sci 265:108886. https://doi.org/10.1016/j.ijmecsci.2023.108886
21. Skeens JW, Kyriakides S (2024) Crushing of a closed-cell polymeric foam under triaxial loading. Int J Solids Struct 291:112686. https://doi.org/10.1016/j.ijsolstr.2024.112686
22. Markaki A, Clyne T (2001) The effect of cell wall microstructure on the deformation and fracture of aluminium-based foams.

Acta Mater 49(9):1677–1686. https://doi.org/10.1016/S1359-6454(01)00072-6
23. Zarei HR, Kröger M (2008) Bending behavior of empty and foam-filled beams: structural optimization. Int J Impact Eng 35(6):521–529. https://doi.org/10.1016/j.ijimpeng.2007.05.003
24. Shen J, Lu G, Ruan D (2010) Compressive behaviour of closed-cell aluminium foams at high strain rates. Compos Part B Eng 41(8):678–685. https://doi.org/10.1016/j.compositesb.2010.07.005
25. Yang X, Xia Y, Zhou Q (2011) Influence of stress softening on energy-absorption capability of polymeric foams. Mater Des 32(3):1167–1176. https://doi.org/10.1016/j.matdes.2010.10.024
26. Hassanli F, Paydar MH (2021) Improvement in energy absorption properties of aluminum foams by designing pore-density distribution. J Mater Res Technol 14:609–619. https://doi.org/10.1016/j.jmrt.2021.06.073
27. Gomez A, Barbero E, Sanchez-Saez S (2022) Modelling of carbon/epoxy sandwich panels with agglomerated cork core subjected to impact loads. Int J Impact Eng 159:104047. https://doi.org/10.1016/j.ijimpeng.2021.104047
28. Liu K, Kang SB, Gao S (2023) Experimental and analytical study on impact response of stainless steel-aluminium foam-alloy steel sandwich panels. Int J Impact Eng 179:104661. https://doi.org/10.1016/j.ijimpeng.2023.104661
29. Jalali SS, Mahzoon M, Mohammadi H (2023) Identification of damage properties of glass/epoxy laminates using machine learning models. Int J Impact Eng 177:104510. https://doi.org/10.1016/j.ijimpeng.2023.104510
30. Stronge WJ (2018) Impact mechanics, 2nd edn. Cambridge University Press, Cambridge. https://doi.org/10.1017/9781139050227
31. Ying L, Wang S, Gao T, Dai M, Hu P, Wang Y (2023) Crashworthiness analysis and optimization of multi-functional gradient foam-aluminum filled hierarchical thin-walled structures. Thin-Walled Struct 189:110906. https://doi.org/10.1016/j.tws.2023.110906
32. Ghamarian A, Zarei HR, Abadi MT (2011) Experimental and numerical crashworthiness investigation of empty and foam-filled end-capped conical tubes. Thin-Walled Struct 49(10):1312–1319. https://doi.org/10.1016/j.tws.2011.03.005
33. Yan W, Durif E, Yamada Y, Wen C (2007) Crushing simulation of foam-filled aluminium tubes. Mater Trans 48(7):1901–1906. https://doi.org/10.2320/matertrans.MRA2007071
34. Kuo Y, Yang T, Huang G-W (2008) The use of a grey-based Taguchi method for optimizing multi-response simulation problems. Eng Optim 40(6):517–528. https://doi.org/10.1080/03052150701857645
35. Liu S, Lin Y (2010) Introduction to Grey systems theory. J Gray Syst. https://doi.org/10.1007/978-3-642-16158-2_1
36. Afsari O, Hashemnia K (2024) Optimized design of a linear vibrating screen based on efficiency maximisation and mesh wear minimisation employing discrete element method. Particuology 90:307–322. https://doi.org/10.1016/j.partic.2024.01.004
37. Fung C, Huang C, Doong J (2003) The study on the optimization of injection molding process parameters with gray relational analysis. J Reinf Plast Compos 22(1):51–66. https://doi.org/10.1106/073168403022843
38. United Nations Agreement (1994) Uniform provisions concerning the approval of vehicles with regards to their front and rear protective devices (Bumpers, etc.). ECE Regulation No. 42
39. Sun G, Wang X, Fang J, Pang T, Li Q (2021) Parallelized optimization design of bumper systems under multiple low-speed impact loads. Thin-Walled Struct 167:108197. https://doi.org/10.1016/j.tws.2021.108197
40. Chang L, Patel Y, Wang H, Williams JG (2016) The Partitioning of Plastic Energy in Cutting Tests. Procedia Struct Integr 2:309–315. https://doi.org/10.1016/j.prostr.2016.06.040
41. Alexopoulos ND, Papanikos P (2008) Experimental and theoretical studies of corrosion-induced mechanical properties degradation of aircraft 2024 aluminum alloy. Mater Sci Eng A 498(1–2):248–257. https://doi.org/10.1016/j.msea.2008.08.024
42. Cronin DS, Ouellet S (2016) Low density polyethylene, expanded polystyrene and expanded polypropylene: strain rate and size effects on mechanical properties. Polym Test 53:40–50. https://doi.org/10.1016/j.polymertesting.2016.04.018
43. Hanssen AG, Girard Y, Olovsson L, Berstad T, Langseth M (2006) A numerical model for bird strike of aluminium foam-based sandwich panels. Int J Impact Eng 32(7):1127–1144. https://doi.org/10.1016/j.ijimpeng.2004.09.004